

X-RAY EMISSION FROM THE WOLF-RAYET BUBBLE S 308*

J.A. TOALÁ^{1,2,†}, M.A. GUERRERO¹, Y.-H. CHU³, R.A. GRUENDL³, S.J. ARTHUR², R.C. SMITH⁴, AND S.L. SNOWDEN⁵

¹ Instituto de Astrofísica de Andalucía, IAA-CSIC, Glorieta de la Astronomía s/n, 18008 Granada, Spain

² Centro de Radioastronomía y Astrofísica, Universidad Nacional Autónoma de México, Campus Morelia, Apartado Postal 3-72, 58090, Morelia, Michoacán, México

³ Department of Astronomy, University of Illinois, 1002 West Green Street, Urbana, IL 61801, USA

⁴ NOAO/CTIO, 950 N. Cherry Avenue, Tucson, AZ 85719, USA and

⁵ NASA Goddard Space Flight Center, Code 662, Greenbelt, MD 20771, USA

Draft version June 20, 2012

ABSTRACT

The Wolf-Rayet (WR) bubble S 308 around the WR star HD 50896 is one of the only two WR bubbles known to possess X-ray emission. We present *XMM-Newton* observations of three fields of this WR bubble that, in conjunction with an existing observation of its Northwest quadrant, map most of the nebula. The X-ray emission from S 308 displays a limb-brightened morphology, with a central cavity $\sim 22'$ in size and a shell thickness of $\sim 8'$. This X-ray shell is confined by the optical shell of ionized material. The spectrum is dominated by the He-like triplets of N VI at 0.43 keV and O VII at 0.57 keV, and declines towards high energies, with a faint tail up to 1 keV. This spectrum can be described by a two-temperature optically thin plasma emission model ($T_1 \sim 1.1 \times 10^6$ K, $T_2 \sim 13 \times 10^6$ K), with a total X-ray luminosity $\sim 2 \times 10^{33}$ erg s⁻¹ at the assumed distance of 1.5 kpc.

Subject headings: ISM: bubbles – ISM: individual (S 308) – stars: individual (HD 50896) – stars: winds, outflows – stars: Wolf-Rayet – X-rays: individual (S 308)

1. INTRODUCTION

Wolf-Rayet (WR) bubbles are the final result of the evolution of the circumstellar medium (CSM) of massive stars with initial masses $M \gtrsim 35 M_\odot$. These stars exhibit high mass-loss rates throughout their lives, peaking during their post-main-sequence evolution that involves a Red or Yellow Supergiant (RSG or YSG) or Luminous Blue Variable (LBV) stage (e.g., Meynet & Maeder 2003) during which the mass-loss rate can be as high as 10^{-4} – $10^{-3} M_\odot \text{ yr}^{-1}$ (Nugis & Lamers 2000), although the stellar wind velocity is low (10 – 10^2 km s⁻¹). The final WR stage is characterized by a fast stellar wind ($v_\infty \gtrsim 10^3$ km s⁻¹), which sweeps up, shocks, and compresses the RSG/LBV material. Thin-shell and Rayleigh-Taylor instabilities lead to the corrugation and eventual fragmentation of the swept-up shell (García-Segura et al. 1996a,b; Freyer et al. 2003, 2006; Toalá & Arthur 2011). Clumpy WR wind-blown bubbles have been detected at optical wavelengths around ~ 10 WR stars in our Galaxy (Chu et al. 1983; Gruendl et al. 2000; Stock & Barlow 2010). Their optical emission is satisfactorily modeled as photoionized dense clumps and shell material (Esteban et al. 1993).

X-ray emission has been detected so far in only two WR bubbles, NGC 6888 and S 308 (Bochkarev 1988; Wrigge et al. 1994, 1998; Wrigge 1999; Chu et al. 2003; Wrigge & Wendker 2002; Wrigge et al. 2005; Zhekov & Park 2011). The most sensitive X-ray observations of a WR bubble are those of the northwest (NW) quadrant of S 308 presented by Chu et al. (2003). Their *XMM-Newton* EPIC-pn X-ray spectrum of S 308

revealed very soft X-ray emission dominated by the N VI He-like triplet at ~ 0.43 keV and declining sharply toward higher energies. This spectrum was fit with a two-temperature optically thin MEKAL plasma emission model, with a cold main component at $kT_1 = 0.094$ keV (i.e., $T_X \sim 1.1 \times 10^6$ K), and a hot secondary component at $kT_2 \sim 0.7$ keV contributing $\leq 6\%$ of the observed X-ray flux. The comparison of the X-ray and optical H α and [O III] images of S 308 showed that the X-ray emission is confined by the ionized shell.

In this paper, we present the analysis of three additional *XMM-Newton* observations of S 308, which, in conjunction with those of the NW quadrant presented by Chu et al. (2003), map 90% of this WR bubble (see §2). In §3 and §4 we discuss the spatial distribution and spectral properties of the X-ray-emitting plasma in S 308, respectively. In §5 we present our results of the X-ray emission from the central star in the WR bubble. A discussion is presented in §6 and summary and conclusions in §7.

2. XMM-NEWTON OBSERVATIONS

The unrivaled sensitivity of the *XMM-Newton* EPIC cameras to large-scale diffuse emission makes them the preferred choice for the observation of S 308. Chu et al. (2003) presented *XMM-Newton* observations of the brightest NW quadrant of S 308 (Wrigge 1999), but the large angular size of S 308 ($\sim 40'$ in diameter) exceeds the field of view of the EPIC camera and a significant fraction of the nebula remained unobserved. To complement these observations, additional *XMM-Newton* observations of three overlapping fields covering the northeast (NE), southwest (SW), and southeast (SE) quadrants of the nebula have been obtained. The previous and new observations result in the coverage of $\sim 90\%$ of the area of S 308. The pointings, dates and revolutions of the ob-

*Based on observations obtained with XMM-Newton, an ESA science mission with instruments and contributions directly funded by ESA Member States and NASA.

[†]toala@iaa.es

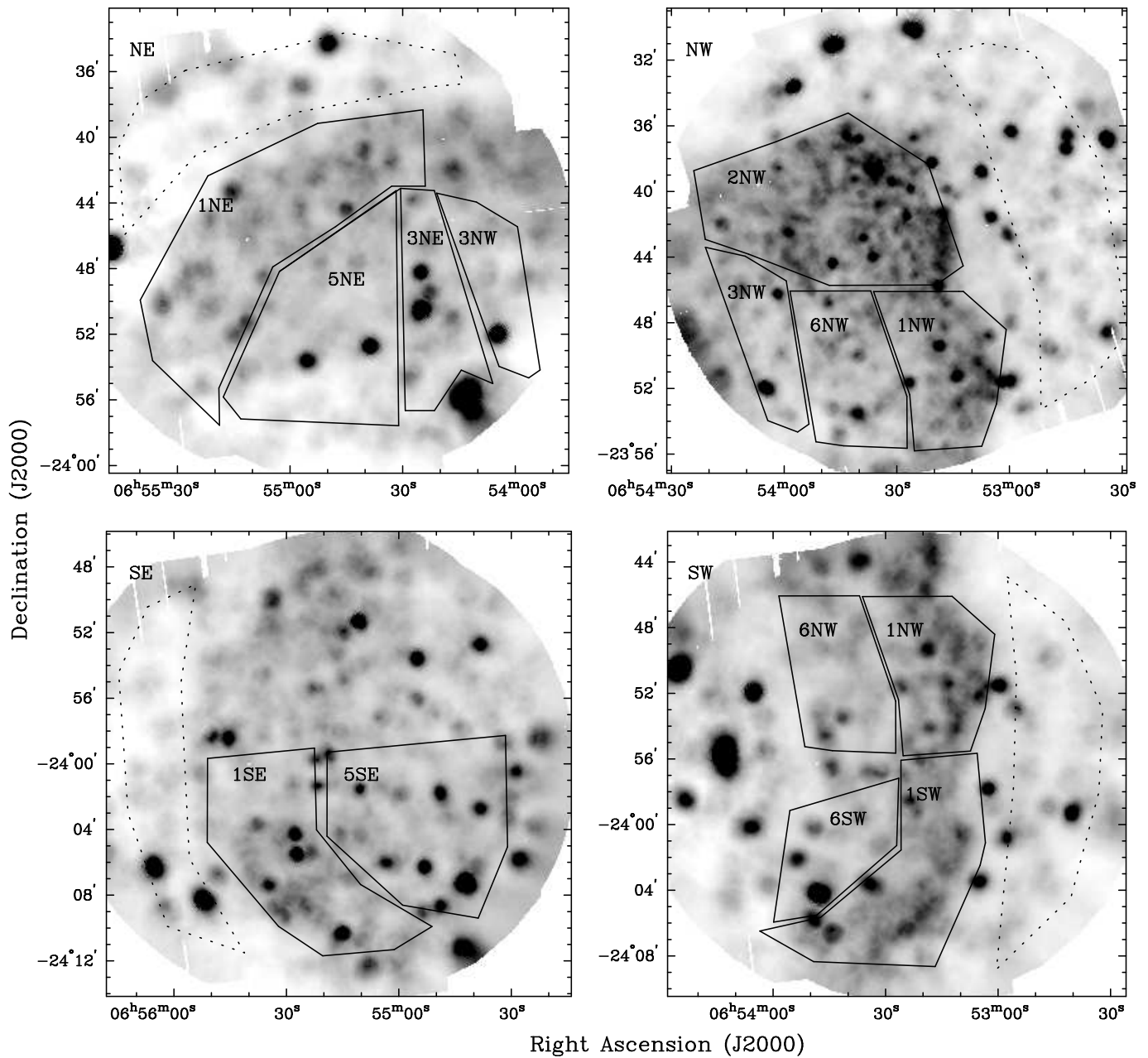


FIG. 1.— *XMM-Newton* EPIC images of the four observations of S 308 in the 0.3–1.15 keV band. The images have been extracted using a pixel size of $2''.0$ and adaptively smoothed using a Gaussian kernel between $5''$ and $30''$. The source regions used for spectral analysis are indicated by solid lines and the background regions by dotted lines. Note that the point sources that are present in the images were excised for the spectral analysis.

servations, and their exposure times are listed in Table 1. In the following, we will refer to the individual observations by the quadrant of S 308 that is covered, namely the NW, NE, SW, and SE quadrants. All observations were obtained using the Medium Filter and the Extended Full-Frame Mode for EPIC-pn and Full-Frame Mode for EPIC-MOS.

The *XMM-Newton* pipeline products were processed using the *XMM-Newton* Science Analysis Software (SAS) Version 11.0, and the Calibration Access Layer available on 2011-09-13. In order to analyze the diffuse and soft X-ray emission from S 308, the *XMM-Newton* Extended Source Analysis Software (XMM-ESAS) package (Snowden et al. 2008; Kuntz & Snowden 2008) has been

used. This procedure applies very restrictive selection criteria for the screening of bad events registered during periods of high background to ensure a reliable removal of the background and instrumental contributions, particularly in the softest energy bands. As a result, the final net exposure times resulting from the use of the XMM-ESAS tasks, as listed in Table 1, are noticeably shorter than the original exposure times. Since we are interested in the best time coverage of the central WR star to assess its possible X-ray variability and given that its X-ray emission level is much brighter than that of a mildly enhanced background, we applied less restrictive criteria in selecting good time intervals for this star. For this particular analysis, the 10–12 keV energy band

TABLE 1
XMM-Newton OBSERVATIONS OF S 308

Pointing	R.A. (J2000)	Dec.	Obs. ID	Rev.	Observation start UTC	Total exposure time			Net exposure time		
						pn [ks]	MOS1 [ks]	MOS2 [ks]	pn [ks]	MOS1 [ks]	MOS2 [ks]
NW	06:53:30	-23:43:00	0079570201	343	2001-10-23T22:00:09	43.5	47.6	47.5	11.9	19.6	19.9
SW	06:53:24	-23:56:18	0204850401	781	2004-03-15T14:30:41	20.0	23.3	23.4	6.4	9.0	9.2
SE	06:55:16	-24:00:00	0204850501	781	2004-03-14T23:00:41	22.0	25.4	25.4	8.2	12.4	12.7
NE	06:54:47	-23:46:18	0204850601	781	2004-03-15T06:45:41	22.0	25.4	25.4	5.4	8.9	8.4

is used to assess the charged particle background, and we excised periods of high background with EPIC-pn count rates ≥ 1.5 counts s^{-1} and EPIC-MOS count rates ≥ 0.3 counts s^{-1} .

3. SPATIAL DISTRIBUTION OF THE DIFFUSE X-RAY EMISSION

3.1. Image processing

Following Snowden & Kuntz' cookbook for analysis procedures for XMM-Newton EPIC observations of extended objects and diffuse background, Version 4.3 (Snowden & Kuntz 2011), the XMM-ESAS tasks and the associated Current Calibration Files (CCF), as obtained from ftp://xmm.esac.esa.int/pub/ccf/constituents/extras/esas_caldb, have been used to remove the contributions from the astrophysical background, soft proton background, and solar wind charge-exchange reactions, which have contributions at low energies (< 1.5 keV). The resulting exposure-map-corrected, background-subtracted EPIC images of each observed quadrant of S 308 in the 0.3–1.15 keV band are presented in Figure 1. The new observations of the NE, SW, and SE quadrants of S 308 detect diffuse emission, as well as a significant number of point sources superimposed on this diffuse emission. With the single exception of HD 50896 (a.k.a. WR 6), the WR star progenitor of this bubble registered in the SW and NE observations, all point sources are either background or foreground sources that we have removed prior to our analysis.

3.2. Analysis of the diffuse X-ray emission

In order to analyze the spatial distribution of the diffuse X-ray emission in S 308, the four individual observations have been mosaicked using the XMM-ESAS tasks and all point sources removed using the Chandra Interactive Analysis of Observations (CIAO) Version 4.3 *dmfilth* routine, except the one corresponding to WR 6. The final image (Figure 2-left), extracted in the 0.3–1.15 keV energy band with a pixel size of $3''0$, has been adaptively smoothed using the ESAS task *adapt-2000* requesting 100 counts of the original image for each smoothed pixel, with typical smoothing kernel scales $\leq 1'$ in the brightest regions and $1' - 2'$ in the faintest ones. This image reveals that the diffuse X-ray emission from S 308 has a limb-brightened morphology, with an irregular inner cavity $\sim 22'$ in size. The surface brightness distribution displayed by this image confirms and adds further details to the results of previous X-ray observations (Wrigge 1999; Chu et al. 2003). The X-ray emission from the bubble is brighter towards the northwest blowout and the western rim, and fainter towards the east. The bubble seems

to lack detectable X-ray emission towards the central regions around the WR star.

The limb-brightened spatial distribution of the X-ray emission from S 308 is further illustrated by the surface brightness profiles along the SE–NW and NE–SW directions shown in Figure 3. The emission in the innermost regions, close to the central WR star, falls to levels comparable to those of a background region to the west of S 308 shown in the bottom panel of Fig. 3. Besides the SE region, whose surface brightness distribution is best described by a plateau, the X-ray emission along the other directions increases steadily with radial distance, peaking near the shell rim and declining sharply outwards. The thickness of the X-ray-emitting shell is difficult to quantify; along the SW direction, it has a FWHM $\sim 5'$, whereas it has a FWHM $\sim 8'$ along the NE direction. Figure 3 also illustrates that the X-ray-emitting shell is larger along the SE–NW direction ($\sim 44'$ in size) than along the NE–SW direction ($\sim 40'$ in size).

Finally, the spatial distribution of the diffuse X-ray emission from S 308 is compared to the [O III] emission from the ionized optical shell in Figure 2-right. The X-ray emission is interior to the optical emission not only for the NW quadrant but for the entire bubble. This is also illustrated in the color composite picture shown in Figure 4, in which the distribution of the X-ray emission is compared to the optical $H\alpha$ and [O III] images. This image shows that the diffuse X-ray emission is closely confined by the filamentary emission in the $H\alpha$ line, whereas the smooth emission in the [O III] line extends beyond both the $H\alpha$ and X-ray rims.

4. PHYSICAL PROPERTIES OF THE HOT GAS IN S 308

The spectral properties of the diffuse X-ray emission from S 308 can be used to investigate the physical conditions and chemical abundances of the hot gas inside this nebula. In order to proceed with this analysis, we have defined several polygonal aperture regions, as shown in Figure 1, which correspond to distinct morphological features of S 308: regions with #1 designations correspond to the rim revealed by the limb-brightened morphology, #2 the NW blowout, #3, #5, and #6 shell interior, and #4 the central star HD 50896. We note that any particular morphological feature may have been registered in more than one quadrant, in which case several spectra can have the same numerical designation (for instance, there are four spectra for the rim of the shell, namely 1NE, 1NW, 1SE, and 1SW).

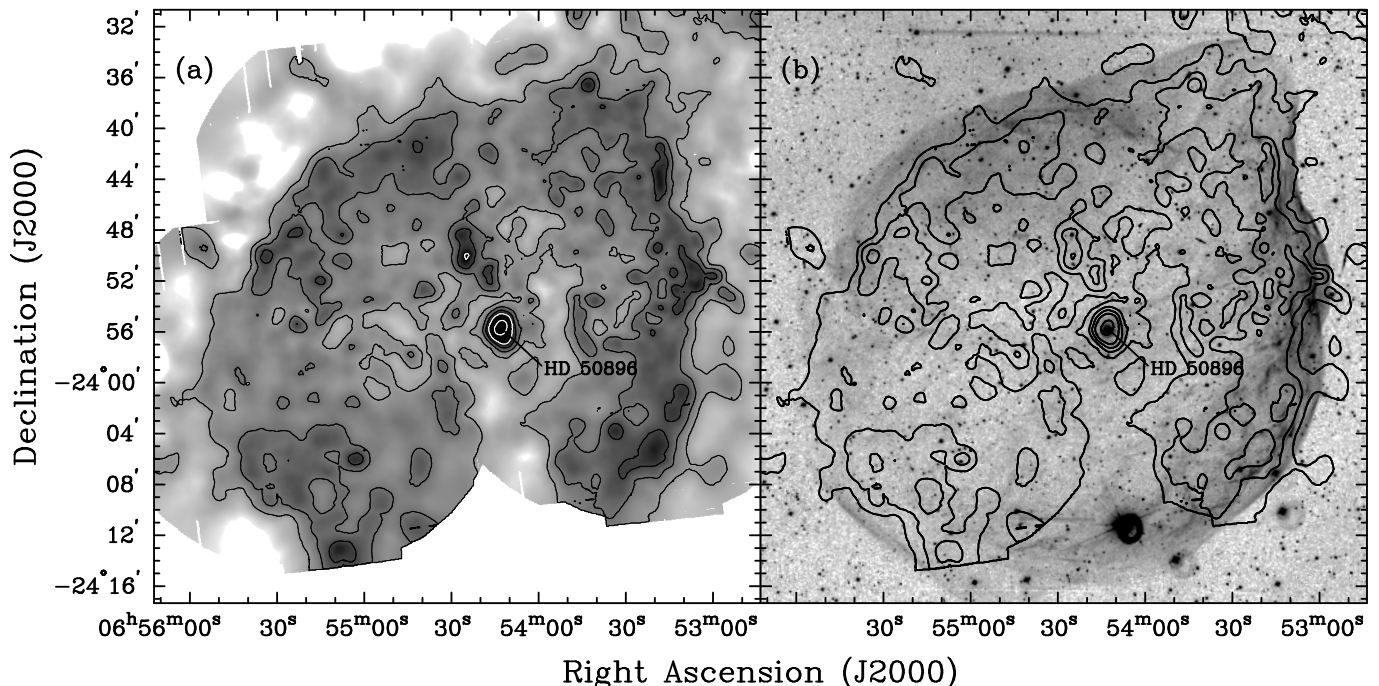


FIG. 2.— (left) Adaptively smoothed *XMM-Newton* EPIC Image of S308 in the 0.3–1.15 keV band. All point sources, except for the central star HD 50896 (WR 6), have been excised. (right) Ground-based [O III] image of S308 obtained with the Michigan Curtis Schmidt telescope at Cerro Tololo Inter-American Observatory (CTIO) with superimposed X-ray emission contours. The position of the central star HD 50896 is indicated in both panels.

4.1. Spectra Extraction and Background Subtraction

Perhaps the most challenging problem associated with the analysis of the X-ray spectra of S308 is a reliable subtraction of the background contribution. The diffuse X-ray emission from S308 fills a significant fraction of the field of view of the EPIC-pn and EPIC-MOS cameras, making the selection of suitable background regions difficult because the instrumental spectral response of the cameras close to their edges may not be the same as those for the source apertures.

The background contribution to the diffuse emission from clusters of galaxies that fills the field of view is typically assessed from high signal-to-noise ratio observations of blank fields. In the case of S308, however, the comparison of spectra extracted from background regions with those extracted from the same detector regions of the most suitable EPIC Blank Sky observations (Carter & Read 2007) clearly indicates that they have different spectral shapes. The reason for this discrepancy lies in the typical high Galactic latitude of the EPIC Blank Sky observations, implying low hydrogen absorption column densities and Galactic background emission, while S308 is located in regions close to the Galactic Plane where extinction and background emission are significant. We conclude that EPIC Blank Sky observations, while suitable for the analysis of the diffuse emission of a large variety of extragalactic objects, cannot be used in our analysis of S308.

Alternatively, the different contributions to the complex background emission in *XMM-Newton* EPIC observations can be modeled, taking into account the contributions from the astrophysical background, solar wind charge-exchange reactions, high-energy (soft protons) particle contributions, and electronic noise. This is the

procedure recommended by the XMM-ESAS in the release of SAS v11.0, following the background modeling methodology devised by Snowden et al. (2004) and Kuntz & Snowden (2008). Even though the modeling of the different contributions is a complex task, it can be routinely carried out. Unfortunately, S308 is projected close to the Galactic Plane and the *ROSAT* All Sky Survey (RASS) reveals that it is located in a region of strong soft background emission with small-scale spatial variations. As shown in Figure 5, the X-ray emission from this background is soft and shows lines in the 0.3–1.0 keV energy band from thermal components as the emission from S308. Therefore, it is not possible to model independently the emission from the S308 bubble and that from the soft background.

The only viable procedure for the analysis seems the use of background spectra extracted from areas near the camera edges of the same observations. It can be expected that the spectral properties of these background spectra differ from those of the background registered by the central regions of the cameras, given the varying spectral responses of the peripheral and central regions of the cameras to the various background components. To assess these differences, we have used EPIC Blank Sky observations to extract spectra from source and background regions identical in detector units to those used for S308. Two typical examples of blank sky background-subtracted spectra are presented in Figure 6. While these spectra are expected to be flat, several deviations can be noticed: (1) clear residuals at ~ 7.5 and ~ 8.1 keV, which can be attributed to the defective removal of the strong instrumental Cu lines that affect the EPIC-pn spectra (Kuntz & Snowden 2008), (2) a noticeable deviation at ~ 0.65 keV of the O-K line, and (3) most notably, deviations at energies below 0.3 keV, which is indicative

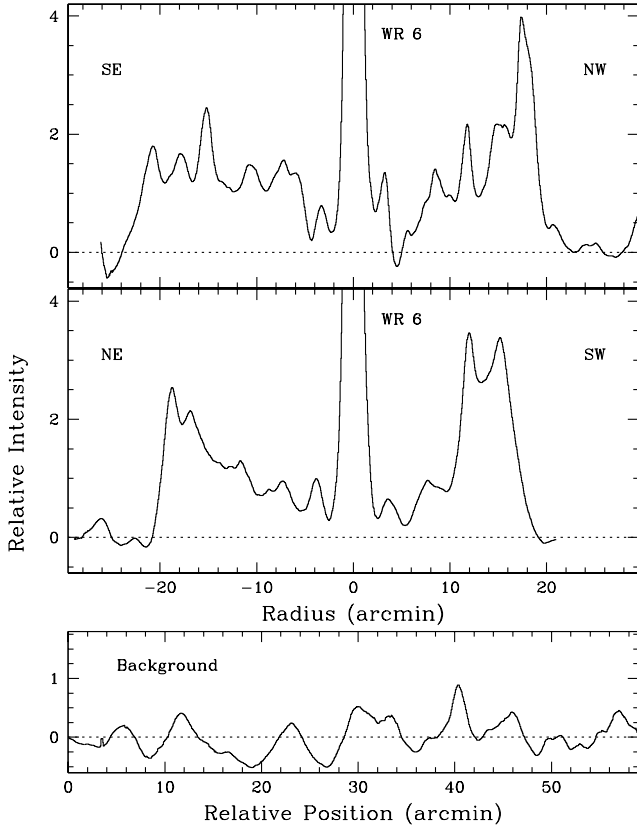


FIG. 3.— S308 X-ray surface brightness profiles along the SE–NW (PA=135°) and SW–NE (PA=45°) directions extracted from the smoothed *XMM-Newton* EPIC image presented in Figure 2-left. For comparison, a surface brightness profile of a representative background region towards the West of S308 is shown at the same intensity and spatial scales.

of the faulty removal of the electronic noise component of the background (Carter & Read 2007). Note that the Al-K line at ~ 1.5 keV and the Si-K line at ~ 1.8 keV, which may be expected to be strong in the background EPIC-pn spectra, are correctly removed. Consequently, we have chosen to use the background spectra extracted from the observations of S308, but restrict our spectral fits to the 0.3–1.3 keV band.

4.2. Spectral properties

The individual background-subtracted EPIC-pn spectra of the diffuse emission of S308 are presented in Figure 7. This figure also includes spectra of the whole nebula, its rim, and central cavity obtained by combining all spectra, those of regions #1 and #2 (the rim or limb-brightened shell), and those of regions #3, #5, and #6 (the central cavity), respectively. Spectra and response and ancillary calibrations matrices from different observations of the same spatial regions were merged using the *mathpha*, *addarf*, and *addrmf* HEASOFT tasks according to the prescriptions of the SAS threads. The EPIC-MOS spectra have also been examined and found to be consistent with the EPIC-pn ones although, due to the lower sensitivity of the EPIC-MOS cameras, they have fewer counts. Therefore, our spectral analysis of the diffuse X-ray emission will concentrate on the EPIC-pn spectra.

The spectra shown in Figure 7 are all soft, with a

prominent peak near $\gtrsim 0.4$ keV, and a rapid decline in emission towards higher energies. Some spectra (e.g., 1NE, 1NW, 1SW, 5NE, and 5SE) show a secondary peak near $\lesssim 0.6$ keV that is only hinted in other spectra. There is little emission above ~ 0.7 keV, although some spectra (e.g., 1SE, 1SW, 2NW, 3NE, 5SE, and 6SW) appear to present a hard component between 0.8 and 1.0 keV.

The feature at ~ 0.4 keV can be identified with the 0.43 keV N VI triplet, while the fainter feature at ~ 0.6 keV can be associated with the 0.57 keV O VII triplet. The occurrence of spectral lines is suggestive of optically thin plasma emission, confirming previous X-ray spectral analyses of S308 (Wrigge 1999; Chu et al. 2003). The predominance of emission from the He-like species of nitrogen and oxygen over their corresponding H-like species implies a moderate ionization stage of the plasma. Furthermore, the relative intensity of the N VI and O VII lines suggests nitrogen enrichment, since the intensity of the O VII lines from a plasma with solar abundances would be brighter than that of the N VI lines.

In accordance with their spectral properties and previous spectral fits of the NW regions of S308 (Chu et al. 2003), all the X-ray spectra of S308 have been fit with XSPEC v12.7.0 (Arnaud 1996) for an absorbed two-temperature APEC optically thin plasma emission model. The absorption model uses Balucińska-Church & McCammon (1992) cross-sections. A low temperature component is used to model the bulk of the X-ray emission, while a high temperature component is used to model the faint emission above 0.7 keV. We have adopted the same chemical abundances as Chu et al. (2003), i.e., C, N, O, Ne, Mg, and Fe to be 0.1, 1.6, 0.13, 0.22, and 0.13 times their solar values (Anders & Grevesse 1989), respectively, which correspond to the nebular abundances. The simulated two-temperature APEC model spectra were then absorbed by an interstellar absorption column and convolved with the EPIC-pn response matrices. The resulting spectra were then compared to the observed spectrum in the 0.3–1.3 keV energy range and χ^2 statistics are used to determine the best-fit models. A minimum of 50 counts per bin was required for the spectral fit. The foreground absorption (N_H), plasma temperatures (kT_1 , kT_2) with $1-\sigma$ uncertainties, and emission measures (EM_1 , EM_2) of the best-fit models are listed in Table 2. The best-fit models are overplotted on the background-subtracted spectra in Figure 7, together with the residuals of the fits. Multi-temperature models do not provide a substantial reduction of the value of the reduced χ^2 of the fit. We note that the values of the reduced χ^2 differ the most from unity for large regions, implying inconsistencies of the relative calibrations across the FoV, but the spectral fits still provide a fair description of the observed spectrum. In the following sections we discuss the spectral fits of the emission from the different morphological components of S308 in more detail.

Spectral fits using models with varying chemical abundances of C, N, and O were also attempted, but they did not provide any statistical improvement of the fit. In particular, models with N/O abundance ratios different from those of the nebula resulted in notably worst quality spectral fits. As noted by other authors (see Chu et al. 2003; Zhekov & Park 2011), an X-ray-emitting plasma with chemical abundances similar to those of the optical



FIG. 4.— Composite color picture of the *XMM-Newton* EPIC image (blue) and CTIO [O III] (green) and $H\alpha$ (red) images of S 308. The apparent X-ray emission outside the optical shell is caused by large fluctuations in the background in regions near the EPIC cameras edge where the net exposure is much shorter than at the aimpoint.

nebulae seems at this moment to be the most adequate model for the soft X-ray emission from WR bubbles.

4.2.1. Properties of the Global X-ray Emission from S 308

The best-fit to the combined spectrum of the whole nebula results in unphysically high values of the hydrogen absorption column density, N_H , well above the range $[0.2 - 1.05] \times 10^{21} \text{ cm}^{-2}$ implied by the optical extinction values derived from Balmer decrement of the nebula (Esteban et al. 1992). The effects of N_H and nitrogen abundance on the χ^2 of the spectral fits appear to be correlated, i.e., models with high N_H and low nitrogen abundance fit the spectra equally well as models with

low N_H and high nitrogen abundance. If we adopt the high absorption column density from the best-fit model ($N_H \gtrsim 3 \times 10^{21} \text{ cm}^{-2}$), the elevated nitrogen abundance reported by Chu et al. (2003) will not be reproduced. As the high absorption column density is not supported by the optical extinction, in the subsequent spectral fits we will adopt a fixed N_H of $6.2 \times 10^{20} \text{ cm}^{-2}$ that is consistent with the optical extinction measurements. We note that this choice results in an imperfect modeling of the spectral features in the 0.3–0.5 keV range, as indicated by the S-shaped distribution of residuals in this spectral region in Fig. 7. If we allow the value of N_H to float during the spectral fit, the improvement of the value of

TABLE 2
SPECTRAL FITS OF THE DIFFUSE X-RAY EMISSION OF S 308

Region	Counts	N_H [10^{20} cm^{-2}]	kT_1 [keV]	EM_1^a [cm^{-3}]	f_1^b [$\text{erg cm}^{-2} \text{ s}^{-1}$]	kT_2 [keV]	EM_2^a [cm^{-3}]	f_2^b [$\text{erg cm}^{-2} \text{ s}^{-1}$]	f_2/f_1	χ^2/DoF
S 308	10290 \pm 19	6.2	0.096 \pm 0.002	7.6 $\times 10^{56}$	2.7 $\times 10^{-12}$	1.12 \pm 0.22	1.2 $\times 10^{55}$	2.4 $\times 10^{-13}$	0.090	2.01 (=319.6/159)
Shell	7920 \pm 23	6.2	0.092 \pm 0.003	4.9 $\times 10^{56}$	1.5 $\times 10^{-12}$	1.54 (=233.9/151)
Interior	2390 \pm 120	6.2	0.116 \pm 0.011	8.3 $\times 10^{55}$	5.6 $\times 10^{-13}$	0.95	4.8 $\times 10^{54}$	7.5 $\times 10^{-14}$	0.134	1.35 (=188.2/139)
1NE	965 \pm 10	6.2	0.094 \pm 0.010	1.7 $\times 10^{56}$	5.1 $\times 10^{-13}$	0.95	1.1 $\times 10^{53}$	2.5 $\times 10^{-15}$	0.005	0.82 (=46.9/57)
1NW	1000 \pm 60	6.2	0.102 \pm 0.009	4.7 $\times 10^{55}$	2.0 $\times 10^{-13}$	0.95	4.4 $\times 10^{50}$	1.0 $\times 10^{-17}$	< 10^{-3}	1.13 (=57.9/51)
1SE	540 \pm 50	6.2	0.094 \pm 0.010	1.8 $\times 10^{56}$	5.1 $\times 10^{-13}$	0.95	1.1 $\times 10^{53}$	2.5 $\times 10^{-15}$	0.005	0.82 (=46.9/57)
1SW	1100 \pm 50	6.2	0.097 \pm 0.012	1.0 $\times 10^{56}$	3.9 $\times 10^{-13}$	0.95	2.3 $\times 10^{54}$	5.2 $\times 10^{-14}$	0.135	1.31 (=69.3/53)
2NW	4620 \pm 100	6.2	0.095 \pm 0.003	2.2 $\times 10^{56}$	7.4 $\times 10^{-13}$	0.96 \pm 0.21	4.3 $\times 10^{54}$	9.8 $\times 10^{-14}$	0.130	1.30 (=137.9/106)
3NE	300 \pm 33	6.2	0.095 \pm 0.023	3.5 $\times 10^{55}$	1.2 $\times 10^{-13}$	0.95	1.4 $\times 10^{54}$	3.1 $\times 10^{-14}$	0.262	0.55 (=9.4/17)
3NW	160 \pm 25	6.2	0.11 \pm 0.04	5.0 $\times 10^{54}$	2.5 $\times 10^{-14}$	0.95	5.6 $\times 10^{51}$	1.2 $\times 10^{-16}$	0.005	0.91 (=27.4/30)
5NE	530 \pm 50	6.2	0.090 \pm 0.015	7.6 $\times 10^{55}$	2.1 $\times 10^{-13}$	0.95	9.0 $\times 10^{53}$	1.8 $\times 10^{-14}$	0.083	1.06 (=44.5/42)
5SE	820 \pm 60	6.2	0.103 \pm 0.016	4.4 $\times 10^{55}$	1.9 $\times 10^{-13}$	0.95	2.2 $\times 10^{54}$	5.1 $\times 10^{-14}$	0.268	1.05 (=54.5/52)
6NW	400 \pm 50	6.2	0.112 \pm 0.015	1.8 $\times 10^{55}$	1.0 $\times 10^{-13}$	1.42 (=50.0/35)
6SW	210 \pm 32	6.2	0.12 \pm 0.05	8.3 $\times 10^{54}$	5.7 $\times 10^{-14}$	0.95	9.7 $\times 10^{53}$	1.5 $\times 10^{-14}$	0.270	1.69 (=27.0/16)
W99 ^c	4560	35	0.129	1.0 $\times 10^{56}$	6.5 $\times 10^{-12}$	2.4	4.3 $\times 10^{55}$	1.2 $\times 10^{-12}$	0.185	20 (=40/2)
C03 ^d	...	11	0.094 \pm 0.009	8.2 $\times 10^{56}$	7.2 $\times 10^{-12}$	0.7 $^{+1.5}_{-0.5}$	5.1 $\times 10^{54}$	1.1 $\times 10^{-13}$	0.015	1.02

^aEM = $\int n_e^2 dV$.

^bObserved (absorbed) fluxes for the two-temperature models components in the energy range 0.3-1.3 keV.

^cWrigge (1999).

^dChu et al. (2003).

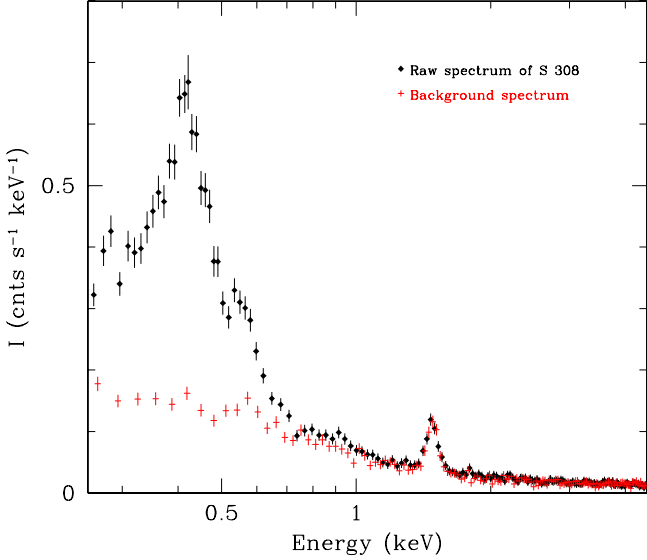


FIG. 5.— Comparison of the background-unsubtracted raw EPIC-pn spectrum of S 308 (black) and scaled EPIC-pn background spectrum (red). The Al-K line at ~ 1.5 keV is an instrumental line.

the reduced χ^2 is negligible.

The parameters of the best-fit model, listed in the first line of Table 2, show two plasma components at temperatures $\sim 1.1 \times 10^6$ K and $\sim 1.3 \times 10^7$ K with an observed flux ratio, $f_2/f_1 \sim 0.09$, corresponding to an intrinsic flux ratio $F_2/F_1 \sim 0.06$. The total observed flux is $\sim 3 \times 10^{-12} \text{ erg cm}^{-2} \text{ s}^{-1}$. The intrinsic luminosity at a distance of 1.5 kpc¹, after accounting for a fraction of $\sim 1/3$ of S 308 which is not included in the source aper-

¹ See discussion about the distance to WR 6 of Chu et al. (2003).

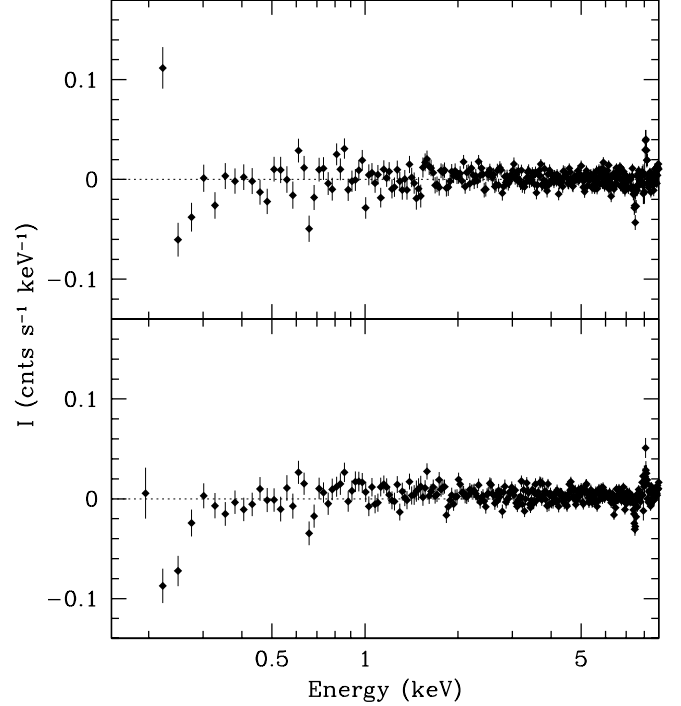


FIG. 6.— Background-subtracted blank sky spectra extracted from source and background regions equal in detector coordinates to the regions 1NW (top) and 1SW (bottom) of S 308.

tures considered here, is $\sim 2 \times 10^{33} \text{ erg s}^{-1}$. The emission measure of the best-fit to the combined spectrum, along with the spatial distribution of the X-ray-emitting gas in a spherical thick shell with a thickness $\sim 8'$ and inner radius of $\sim 11'$, implies an average electron density $n_e \sim 0.1 \text{ cm}^{-3}$. We note that the quality of the spectral fit is not exceptionally good, but more sophisticated fits using multi-temperature models failed to improve the

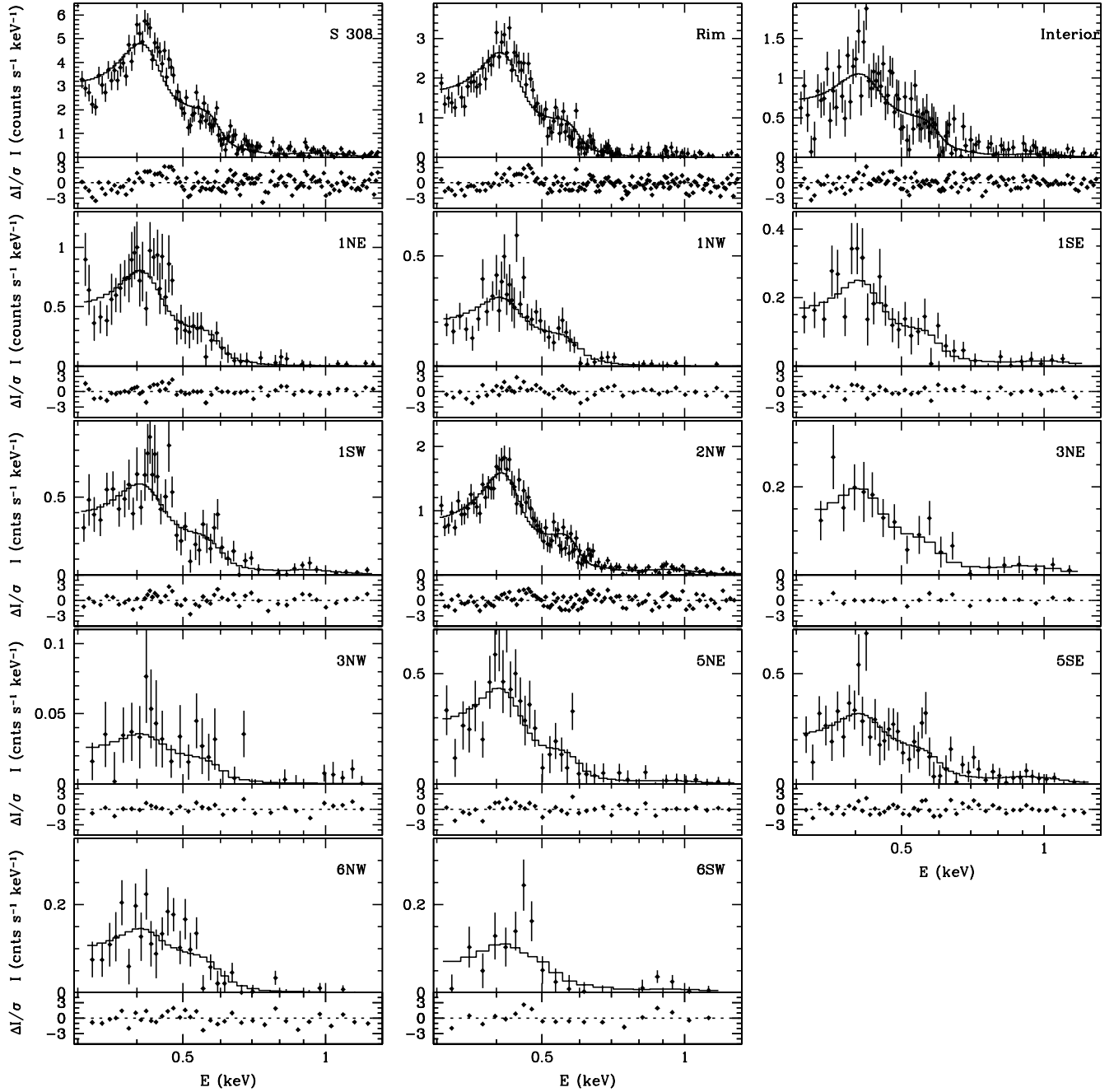


FIG. 7.— Background-subtracted *XMM-Newton* EPIC-pn spectra of S308 corresponding to the 11 individual source regions shown in Figure 1, as well as the combined spectra of the entire nebula, its shell or rim (regions #1 and #2) and the interior region of the shell (#3, #5, and #6). Each spectrum is overplotted with its best-fit two-temperature APEC model in the energy range 0.3–1.3 keV, assuming fixed abundances, while the lower panel displays the residuals of the fit.

quality of the fit. The proposed 2-T model, providing a fair description of the spectral shape, should be considered as a first approximate of the hot gas content and its physical conditions.

4.2.2. Northwest Blowout (Region #2)

The northwest blowout of S308 has the brightest X-ray emission, with a surface brightness $\sim 2.0 \times 10^{-18} \text{ erg cm}^{-2} \text{ s}^{-1} \text{ arcsec}^{-2}$ and its individual spectrum

has a high signal-to-noise ratio. The spectral shape is consistent with those of the shell spectra, with a prominent 0.43 keV N VI line, a weaker O VII line, and a clear detection of X-ray emission to energies of 0.8–1.0 keV. The best-fit parameters are rather similar to those of the spectrum of the entire nebula, with a marginally lower temperature for the hard component. We will adopt this value of the hard component temperature for those regions whose spectra do not have an adequate count number to fit this parameter.

4.2.3. The Limb-Brightened Shell

The diffuse X-ray emission from S 308 has a clear limb-brightened morphology surrounding a cavity of diminished X-ray surface brightness. The emission from regions at the rim of this shell (1NE, 1NW, 1SE, and 1SW) is relatively bright, with an averaged surface brightness of the rim $\sim 1.2 \times 10^{-18} \text{ erg cm}^{-2} \text{ s}^{-1} \text{ arcsec}^{-2}$. All individual spectra of the rim regions show the bright 0.43 keV N VI emission line and indications of the weaker 0.57 keV O VII emission line. The hard component is faint, except for the spectrum of region 1SW. The fit to the combined spectrum confirms the temperature of the soft component, but it is not possible to provide statistical proof of the detection of the hard component. The fits to the individual spectra only provide upper limits for this component, except for region 1SW where it seems relatively bright.

4.2.4. The Central Cavity

The level of X-ray emission from the innermost regions of the optical shell of S 308 is lower than that of its edge, with an averaged surface brightness of $5 \times 10^{-19} \text{ erg cm}^{-2} \text{ s}^{-1} \text{ arcsec}^{-2}$, i.e., ~ 2.5 – 4.0 times fainter than the shell and blowout regions. The combined X-ray spectrum of the interior regions shown in Figure 7 indicates a stronger relative contribution from the hard component. This is indeed confirmed by the spectral fit: on average, the hard X-ray component has a flux $\sim 13\%$ that of the soft component. There is a noticeable lack of emission from this component in the region 6NW, but otherwise the average contributions derived from the individual fits are higher than for the spectra of apertures on the shell rim.

4.2.5. Comparison with Previous X-ray Studies

Table 2 also lists the best-fit parameters of the spectral fits to the diffuse X-ray emission from S 308 obtained by Wrigge (1999) and Chu et al. (2003). It is worthwhile discussing some of the differences with these previous X-ray analyses. The Chu et al. (2003) joint fit of our regions 1NW, 2NW, 3NW and 6NW yields very similar results to the ones shown in Table 2. For the second thermal component, the derived temperatures from our spectral fits and those of Chu et al. (2003) are consistent with each other, but Wrigge (1999) provides a much higher temperature for this component. This discrepancy highlights the difficulty of fitting the hard component using *ROSAT* PSPC data given its low spectral resolution, as well as the very likely contamination of the *ROSAT* PSPC spectrum of S 308 by unresolved hard point sources superposed on the diffuse emission.

5. THE CENTRAL STAR WR6 (HD 50896)

The central star of S 308 is WR 6 (a.k.a. HD 50896), which has a spectral subtype WN4 (van der Hucht et al. 1988). The star is detected by the *XMM-Newton* EPIC cameras in the NE and SW pointings of the nebula. The EPIC-pn, EPIC-MOS1, and EPIC-MOS2 count rates are $160 \pm 4 \text{ counts ks}^{-1}$, $65 \pm 2 \text{ counts ks}^{-1}$, and $65 \pm 2 \text{ counts ks}^{-1}$, respectively, from the NE observation, and $141 \pm 4 \text{ counts ks}^{-1}$, $53 \pm 2 \text{ counts ks}^{-1}$, and $52 \pm 2 \text{ counts ks}^{-1}$, respectively, from the SW observation using a source aperture of $50''$ in radius. These

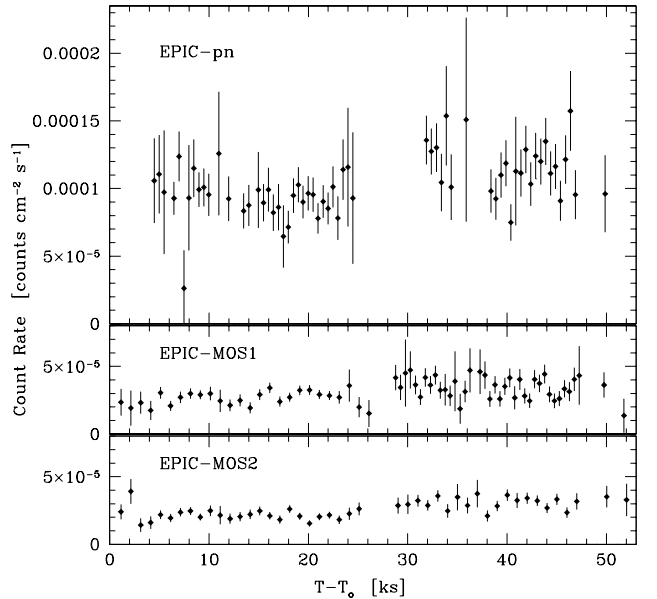


FIG. 8.— EPIC-pn (top), MOS1 (center), and MOS2 (bottom) exposure-map-corrected light curves of WR 6 in the 0.2–9.0 keV energy band. The time is referred to the starting time of the NE observation, 2004-03-15T06:45:41 UTC.

count rates appear to imply that the X-ray luminosity of WR 6 diminished by 10–20% from the NE to the SW observations, which were only ~ 8 hours apart². We note, however, that these count rates are largely affected by vignetting due to the offset position of WR 6 on the EPIC cameras. Indeed, the light curves shown in Figure 8, after accounting for the effects of vignetting, may imply the opposite, i.e., that the X-ray flux of WR 6 was slightly higher in the second (SW) observation than in the first (NE) observation.

In Figure 9 we present the EPIC background-subtracted spectra for the two different epochs. Following Skinner et al. (2002), we have modeled these spectra with a two-temperature VAPEC model with initial abundances set to those shown in Table 1 of van der Hucht et al. (1986). The fit allowed the foreground absorption column density, temperatures, and abundances of N, Ne, Mg, Si, and Fe to vary (Skinner et al. 2002). Table 3 displays the parameters resulting from our best-fit models: absorption column densities N_H , plasma temperatures T , normalization parameters A^3 , observed (absorbed) fluxes f , and intrinsic (unabsorbed) fluxes F . Model fits for the spectra from the NE and SW observations are listed separately alongside those from Skinner et al. (2002) for comparison. The column density and temperatures of the two components are within $1\text{-}\sigma$ of one another among the three different models. The observed fluxes are also consistent, although the Skinner et al. (2002) flux seems to be a bit lower, while our fluxes are closer to the ones derived from the

² The on-axis *XMM-Newton* images presented by Skinner et al. (2002) revealed a faint X-ray source at a radial distance of $\sim 57''$ from WR 6. The flux from this source is $(2 \pm 1)\%$ that of WR 6 and thus it is not likely that fraction of the emission from this source entering into the aperture used for WR 6 would contribute significantly to the observed X-ray variability.

³ $A = 1 \times 10^{-14} \int n_e^2 dV / 4\pi d^2$, where d is the distance, n_e is the electron density, and V the volume in cgs units.

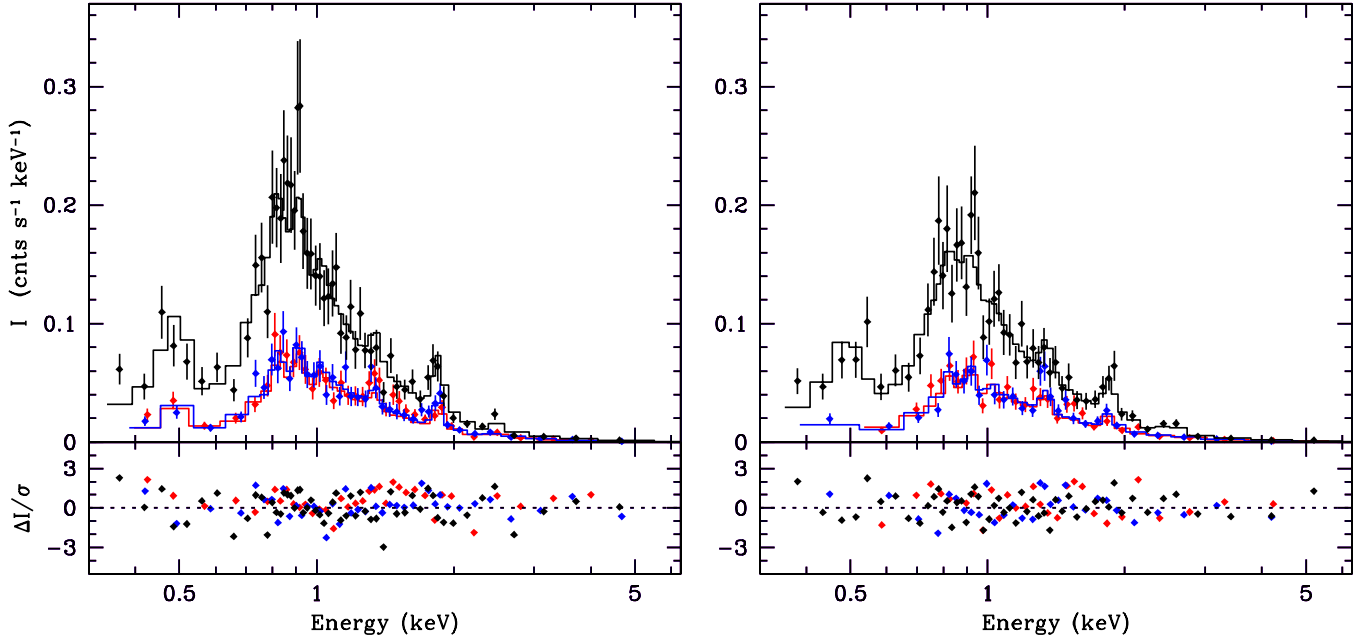


FIG. 9.— Background-subtracted *XMM-Newton* EPIC-pn (black), MOS1 (red), and MOS2 (blue) spectra of WR 6 obtained during the observation of the NE (left) and SW (right) pointings of S 308.

TABLE 3
SPECTRAL FITS OF HD 50896

Parameter	NE Spectrum	SW Spectrum	Skinner et al. (2002)
N_H [$\times 10^{21}$ cm $^{-2}$]	$6.4^{+1.0}_{-0.9}$	$5.9^{+1.2}_{-0.9}$	$4.0^{+0.4}_{-0.6}$
kT_1 [keV]	$0.28^{+0.03}_{-0.04}$	0.28	$0.6^{+0.4}_{-0.4}$
A_1 [cm $^{-5}$]	7.1×10^{-3}	5.9×10^{-3}	3.4×10^{-5}
kT_2 [keV]	$2.5^{+1.5}_{-0.5}$	2.48	$3.5^{+0.7}_{-0.5}$
A_2 [cm $^{-5}$]	1.8×10^{-4}	2.2×10^{-4}	1.0×10^{-5}
χ^2/DoF	1.10=137.0/124	1.10=113.2/103	1.08=234.5/217
f_1 (0.2–10 keV) [$\times 10^{-12}$ erg cm $^{-2}$ s $^{-1}$]	1.14	1.23	0.97
f_1 (2.5–10 keV) [$\times 10^{-12}$ erg cm $^{-2}$ s $^{-1}$]	0.33	0.39	0.31
f_2 (0.2–10 keV) [$\times 10^{-12}$ erg cm $^{-2}$ s $^{-1}$]	0.58	0.70	0.49
F_1 (0.2–10 keV) [$\times 10^{-12}$ erg cm $^{-2}$ s $^{-1}$]	19.8	17.6	2.90
F_1 (2.5–10 keV) [$\times 10^{-12}$ erg cm $^{-2}$ s $^{-1}$]	0.35	0.41	0.33
F_2 (0.2–10 keV) [$\times 10^{-12}$ erg cm $^{-2}$ s $^{-1}$]	1.10	1.35	0.78

October 1995 *ASCA* observations of WR 6 (Skinner et al. 1996). The total observed fluxes and the observed fluxes of the hot thermal component, f_2 , listed in Table 3 may indicate a hardening of the X-ray emission from WR 6 during the last observation. To assess this issue, we performed statistical evaluation of the lightcurves showed in Figure 8 using the HEASOFT task *lcstats* and found no significant variations. Thus, WR 6 does not show evidence of variability in time-scales of hours.

We would like to point out that the absorption column density obtained from our best fits are in good agreement with the values obtained from Skinner et al. (2002), which are higher than that used to fit the soft X-ray emission from the nebula. Such higher column density values are commonly observed towards massive stars such as WR stars and are recognized to be caused by absorption at the base of the wind (Cassinelli et al. 1981; Corcoran et al. 1994; Nazé 2009; Skinner et al. 2010; Gosset et al. 2011).

6. DISCUSSION

The *XMM-Newton* images and spectra analyzed in the previous sections reveal that the hot plasma in S 308 is spatially distributed in a thick shell plus the northwest blowout, with most emission being attributable to a hot plasma at $\sim 1.1 \times 10^6$ K. For an adiabatically shocked stellar wind, its temperature is determined by the stellar wind velocity, $kT = 3\mu m_H V_w^2/16$, where μ is the mean particle mass for fully ionized gas (Dyson & Williams 1997). Therefore, the temperature expected for the shocked stellar wind of WR 6, with a terminal wind velocity of 1700 km s $^{-1}$ (Hamann & Koesterke 1998) and $\mu \gtrsim 1.3$ (van der Hucht et al. 1986), would be $T > 8 \times 10^7$ K, in sharp contrast with the observed temperature. The same issue has been pointed out for the WR bubble NGC 6888 by several authors (see Zhekov & Park 2011, and references therein), and it is also a common issue in planetary nebulae (e.g., NGC 6543; Chu et al. 2001).

Electron thermal conduction has been proposed as a mechanism capable of reducing the temperature of the hot plasma in shocked stellar wind bubbles. Thermal conduction was applied by Weaver et al. (1977) to stellar wind bubbles to produce a self-similar solution for the density and temperature structure in bubbles. The soft X-ray luminosities predicted by Weaver et al.'s model for the Omega Nebula and the Rosette Nebula, according to the stellar wind parameters of their associated young clusters (M17 and NGC 2244, respectively), are several orders of magnitude higher than those observed (Townsend et al. 2003; Dunne et al. 2003). Thus, the standard Weaver et al. model for a stellar wind bubble with thermal conduction cannot be taken at face value. Recent work by Steffen et al. (2008) in the context of planetary nebulae, which are produced in a very similar manner to WR wind bubbles, has calculated the time-dependent radiation-hydrodynamic evolution of planetary nebula wind bubbles including thermal conduction in 1D models with spherical symmetry. In these models, the cold shell material from the previous AGB superwind phase is evaporated into the hot bubble. Saturated conduction was taken into account in these calculations by limiting the electron mean free path and it was found that thermal conduction was able to lower the temperature and raise the density at the edge of the hot bubble enough to explain the soft X-ray emission and low X-ray luminosities observed in some planetary nebulae (e.g., Chu et al. 2001).

In the case of WR bubbles, Toalá & Arthur (2011) presented time-dependent 2D radiation-hydrodynamic models of the evolution of the CSM around single massive stars, including classical and saturated thermal conduction. They found that in the absence of a magnetic field, thermal conduction does not seem to play an important role in shaping WR bubbles, but that models with thermal conduction have slightly greater soft-band luminosities than those without thermal conduction. They suggested that the morphology of S 308 could result from a star with initial mass of $40 M_{\odot}$ whose stellar evolution model includes stellar rotation (Meynet & Maeder 2003). They obtained that $\sim 20,000$ yr after the onset of the WR phase, the X-ray-emitting gas will present a clump-like morphology with an electron density of $n_e \sim 0.1 \text{ cm}^{-3}$ inside an optical ($T \sim 10^4 \text{ K}$) shell with radius of $\sim 9 \text{ pc}$.

Whereas the Toalá & Arthur (2011) models reproduce the morphology and X-ray luminosity of wind-blown bubbles, their simulations predict higher temperatures of the hot plasma that result in X-ray spectra that do not match the observed spectral shape. This might imply that additional physical processes must be taken into account. An interesting alternative to thermal conduction for the apparently low ionization state of the plasma is non-equilibrium ionization (NEI). Smith & Hughes (2010) calculate the timescales to reach collisional ion-

ization equilibrium (CIE) for ionized plasmas and their results suggest that, for values of the parameters relevant to S 308 (derived electron density and time in the WR stage; Toalá & Arthur 2011), the CIE assumptions may not hold. These ideas will be pursued in subsequent works.

7. SUMMARY AND CONCLUSIONS

We present *XMM-Newton* observations of three fields of the WR bubble S 308 which, in conjunction with the observation of its NW quadrant presented by Chu et al. (2003), map most of the nebula except for its southernmost section. We have used these observations to study the spatial distribution of the X-ray-emitting material within this bubble, to derive global values for its physical conditions (T_e , n_e), and to search for their spatial variations among different morphological components of the nebula.

The X-ray emission from S 308 is found to have a limb-brightened morphology, with a shell thickness $5' - 8'$, and extend to the northwest blowout region. The X-ray-emitting shell is notably larger along the SE-NW direction than along the SW-NE direction, and it is always confined by the optical shell of ionized material. The X-ray surface brightness decreases notably from the blowout region and the western rim shell to the shell interior, where the X-ray emission falls to background levels. The western quadrants are also brighter than the eastern quadrants.

The X-ray emission from S 308 shows prominent emission from the He-like triplet of N VI at 0.43 keV and fainter emission of the O VII 0.57 keV triplet, and declines towards high energies, with a faint tail up to 1 keV. This spectrum can be described by a two-temperature optically thin plasma emission model with temperatures $\sim 1.1 \times 10^6 \text{ K}$ and $\sim 1.3 \times 10^7 \text{ K}$. The latter component is notably fainter than the former by at least a factor of ~ 6 . There is an appreciable difference in the relative contributions of the hot component to the X-ray-emitting gas between the rim and the nebula interior, of which the latter has a higher contribution from the hard component. The total X-ray luminosity is estimated to be $\sim 2 \times 10^{33} \text{ erg s}^{-1}$ for a distance of 1.5 kpc.

This research was supported by the NASA *XMM-Newton* Guest Observer Program Grant NNG 04GH99G. SJA and JAT acknowledge financial support from DGAPA-UNAM through grant PAPIIT IN100309. JAT also thanks CONACyT, CONACyT-SNI (Mexico) and CSIC JAE-PREDOC (Spain) for a student grant. JAT and MAG are partially funded by grant AYA2001-29754-C03-02 of the Spanish Ministerio de Economía y Competitividad.

REFERENCES

- Anders, E., & Grevesse, N. 1989, *Geochim. Cosmochim. Acta*, 53, 197
- Arnal, E. M., & Cappa, C. E. 1996, *MNRAS*, 279, 788
- Arnaud, K. A. 1996, *Astronomical Data Analysis Software and Systems V*, 101, 17
- Balucińska-Church, M., & McCammon, D. 1992, *ApJ*, 400, 699
- Bochkarev, N. G. 1988, *Nature*, 332, 518
- Carter, J. A., & Read, A. M. 2007, *A&A*, 464, 1155
- Cassinelli, J. P., Waldron, W. L., Sanders, W. T., et al. 1981, *ApJ*, 250, 677
- Chu, Y.-H. 2008, *IAU Symposium*, 250, 341
- Chu, Y.-H., Guerrero, M. A., Gruendl, R. A., Williams, R. M., & Kaler, J. B. 2001, *ApJ*, 553, L69
- Chu, Y.-H., Guerrero, M. A., Gruendl, R. A., García-Segura, G., & Wendker, H. J. 2003, *ApJ*, 599, 1189
- Chu, Y.-H., Treffers, R. R., & Kwitter, K. B. 1983, *ApJS*, 53, 937

- Corcoran, M. F., Waldron, W. L., Macfarlane, J. J., et al. 1994, *ApJ*, 436, L95
- Cowie, L. L., & McKee, C. F. 1977, *ApJ*, 211, 135
- Dorland, H., & Montmerle, T. 1987, *A&A*, 177, 243
- Dunne, B. C., Chu, Y.-H., Chen, C.-H. R., Lowry, J. D., Townsley, L., Gruendl, R. A., Guerrero, M. A., & Rosado, M. 2003, *ApJ*, 590, 306
- Dyson, J. E., & Williams, D. A. 1997, *The physics of the interstellar medium* (2nd ed.; Bristol: Institute of Physics Publishing)
- Eggleton, P. P. 1971, *MNRAS*, 151, 351
- Eldridge, J. J., & Tout, C. A. 2004, *MNRAS*, 353, 87
- Esteban, C., Vilchez, J. M., Smith, L. J., & Clegg, R. E. S. 1992, *A&A*, 259, 629
- Esteban, C., Smith, L. J., Vilchez, J. M., & Clegg, R. E. S. 1993, *A&A*, 272, 299
- Freyer, T., Hensler, G., & Yorke, H. W. 2003, *ApJ*, 594, 888
- Freyer, T., Hensler, G., & Yorke, H. W. 2006, *ApJ*, 638, 262
- García-Segura, G., Mac Low, M.-M., & Langer, N. 1996a, *A&A*, 305, 229
- García-Segura, G., Langer, N., & Mac Low, M.-M. 1996b, *A&A*, 316, 133
- Gosset, E., De Becker, M., Nazé, Y., et al. 2011, *A&A*, 527, A66
- Gruendl, R. A., Chu, Y.-H., Dunne, B. C., & Points, S. D. 2000, *AJ*, 120, 2670
- Hamann, W.-R., Gräfener, G., & Liermann, A. 2006, *A&A*, 457, 1015
- Hamann, W.-R., & Koesterke, L. 1998, *A&A*, 333, 251
- Kuntz, K. D., & Snowden, S. L. 2008, *A&A*, 478, 575
- Meynet, G., & Maeder, A. 2003, *A&A*, 404, 975
- Nazé, Y. 2009, *A&A*, 506, 1055
- Nugis, T., & Lamers, H. J. G. L. M. 2000, *A&A*, 360, 227
- Pols, O. R., Tout, C. A., Eggleton, P. P., & Han, Z. 1995, *MNRAS*, 274, 964
- Sarazin, C. L. 1988, *X-ray emission from clusters of galaxies*, Cambridge Astrophysics Series, Cambridge: Cambridge University Press, 1988
- Skinner, S., Nagase, F., Ozawa, H., & Itoh, M. 1996, *Bulletin of the American Astronomical Society*, 28, 1375
- Skinner, S. L., Zhekov, S. A., Güdel, M., & Schmutz, W. 2002, *ApJ*, 579, 764
- Skinner, S. L., Zhekov, S. A., Güdel, M., Schmutz, W., & Sokal, K. R. 2010, *AJ*, 139, 825
- Smith, R. K., & Hughes, J. P. 2010, *ApJ*, 718, 583
- Snowden, S. L., Egger, R., Freyberg, M. J., McCammon, D., Plucinsky, P. P., Sanders, W. T., Schmitt, J. H. M. M., Trümper, J., & Voges, W. 1997, *ApJ*, 485, 125
- Snowden, S. L., Collier, M. R., & Kuntz, K. D. 2004, *ApJ*, 610, 1182
- Snowden, S. L., Mushotzky, R. F., Kuntz, K. D., & Davis, D. S. 2008, *A&A*, 478, 615
- Snowden, S. L., & Kuntz, K. D. 2011, *Bulletin of the American Astronomical Society*, 43, #344.17
- Steffen, M., Schönberner, D., & Warmuth, A. 2008, *A&A*, 489, 173
- Stock, D. J., & Barlow, M. J. 2010, *MNRAS*, 409, 1429
- Toalá, J. A., & Arthur, S. J. 2011, *ApJ*, 737, 100
- Townsley, L. K., Feigelson, E. D., Montmerle, T., Broos, P. S., Chu, Y.-H., & Garmire, G. P. 2003, *ApJ*, 593, 874
- van der Hucht, K. A., Cassinelli, J. P., & Williams, P. M. 1986, *A&A*, 168, 111
- van der Hucht, K. A., Hidayat, B., Admiranto, A. G., Supelli, K. R., & Doom, C. 1988, *A&A*, 199, 217
- Weaver, R., McCray, R., Castor, J., Shapiro, P., & Moore, R. 1977, *ApJ*, 218, 377
- Wrigge, M., Wendker, H. J., & Wisotzki, L. 1994, *A&A*, 286, 219
- Wrigge, M., Chu, Y.-H., Magnier, E. A., & Kamata, Y. 1998, *IAU Colloq. 166: The Local Bubble and Beyond*, 506, 425
- Wrigge, M. 1999, *A&A*, 343, 599
- Wrigge, M., & Wendker, H. J. 2002, *A&A*, 391, 287
- Wrigge, M., Chu, Y.-H., Magnier, E. A., & Wendker, H. J. 2005, *ApJ*, 633, 248
- Zhekov, S. A., & Park, S. 2011, *ApJ*, 728, 135